

V4C3TxMXene : a promising active substrate for reactive surface modification and the enhanced electrocatalytic oxygen evolution activity

Du, Cheng - Feng; Sun, Xiaoli; Yu, Hong; Fang, Wei; Jing, Yao; Wang, Yonghui; Li, Shuiqing; Liu, Xianhu; Yan, Qingyu

2020

Du, C.-F., Sun, X., Yu, H., Fang, W., Jing, Y., Wang, Y., . . . Yan, Q. (2020). V4C3TxMXene : a promising active substrate for reactive surface modification and the enhanced electrocatalytic oxygen evolution activity. *InfoMat*, 2(5), 950-959. doi:10.1002/inf2.12078

<https://hdl.handle.net/10356/146096>

<https://doi.org/10.1002/inf2.12078>

© 2020 The Authors. *InfoMat* published by John Wiley & Sons Australia, Ltd on behalf of UESTC. This is an open access article under the terms of the Creative Commons Attribution License, which permits use, distribution and reproduction in any medium, provided the original work is properly cited.

Downloaded on 28 Aug 2022 03:28:29 SGT

ORIGINAL ARTICLE

V₄C₃T_x MXene: A promising active substrate for reactive surface modification and the enhanced electrocatalytic oxygen evolution activity

Cheng-Feng Du^{1,2}  | Xiaoli Sun³ | Hong Yu¹ | Wei Fang⁴ | Yao Jing¹ | Yonghui Wang¹ | Shuiqing Li³ | Xianhu Liu² | Qingyu Yan⁴ 

¹State Key Laboratory of Solidification Processing, Center of Advanced Lubrication and Seal Materials, Northwestern Polytechnical University, Shaanxi, China

²Key Laboratory of Materials Processing and Mold, Zhengzhou University, Ministry of Education, Zhengzhou, China

³Department of Energy and Power Engineering, Tsinghua University, Beijing, China

⁴School of Materials Science and Engineering, Nanyang Technological University, Singapore, Singapore

Correspondence

Shuiqing Li, Department of Energy and Power Engineering, Tsinghua University, Beijing 100084, China.
Email: lishuiqing@mail.tsinghua.edu.cn

Xianhu Liu, Key Laboratory of Materials Processing and Mold, Zhengzhou University, Ministry of Education, Zhengzhou 450002, China.
Email: xianhu.liu@zzu.edu.cn

Qingyu Yan, School of Materials Science and Engineering, Nanyang Technological University, 50 Nanyang Avenue, Singapore 639798, Singapore.
Email: alexyan@ntu.edu.sg

Funding information

Initiative Postdocs Supporting Program, Grant/Award Number: BX20190281; Ministry of Education of Singapore, Grant/Award Numbers: MOE2017-T2-2-069, MOE2018-T2-1-010; National Natural Science Foundation of China, Grant/Award Number: 51901189; Opening Project of Key Laboratory of Materials Processing and Mold, Grant/Award Number: NERC201903

Abstract

Presented are the synthesis, characterizations, and reactive surface modification (RSM) of a novel nine atomic layered V₄C₃T_x MXene. With the advantages of the multilayered V₄C₃T_x MXene that can simultaneously support the RSM reaction and keep the inner skeleton stable, a series of amorphous Ni/Fe/V-ternary oxide hydroxides thin layer can be successfully modified on the surface of the V₄C₃T_x MXene (denoted as MOOH @V₄C₃T_x, M = Ni, Fe, and V) without disrupting its original structure. Attributed to the in situ reconstruction of highly active oxide hydroxide layer, the nanohybrids exhibited an enhanced oxygen evolution reaction (OER) activity and excellent long-time stability over 70 hours. In particular, a current density of 10 mA cm⁻² can be reached by the nanohybrid with the optimized Ni/Fe ratio at an overpotential (η) as low as 275.2 mV, which is comparable to most of the state-of-the-art OER catalysts and better than other MXene-based derivatives. Demonstrated by the tunable physicochemical properties and excellent structural stability of these nanohybrids, we may envision the promising role of the M₄X₃-based MXenes as substrates for a wide range of energy conversion and storage materials.

KEYWORDS

2D material, electrocatalysis, MXene, OER, surface modification

Cheng-Feng Du and Xiaoli Sun contributed equally to this study.

This is an open access article under the terms of the Creative Commons Attribution License, which permits use, distribution and reproduction in any medium, provided the original work is properly cited.

© 2020 The Authors. *InfoMat* published by John Wiley & Sons Australia, Ltd on behalf of UESTC.

With the increasing demands for renewable clean energy, electrocatalytic water splitting techniques that involve both hydrogen evolution reaction and oxygen evolution reaction (OER) have gained growing attention in recent years.¹⁻⁵ However, due to the sluggish reaction kinetics and the large overpotential, gaining further promotion in OER reactivity is still challenging.^{6,7} Recently, some researchers have unlocked the potential of metal oxide hydroxides as an effective catalyst for OER performance.^{6,8-10} However, there is still no ground breakthrough for metal oxide hydroxides until now because of their inferior electronic conductivity. Therefore, the integration of metal oxide hydroxides with highly conductive two-dimensional (2D) materials becomes one of the most effective strategies.^{7,11} On the other hand, MXenes, as a newly developed 2D metal carbide/nitride family, present attractive alternatives to metal oxide hydroxides for OER thanks to their adjustable chemical composition and abundant surface functional groups.¹² Considering their large surface area and excellent electronic conductivity, MXenes have great potential to be used in electrochemical energy conversion and storage applications.¹³⁻¹⁵ However, MXenes consisting of early transition metals usually possess low intrinsic electrocatalytic OER activities.¹⁶⁻¹⁸ One option being researched to compensate the aforementioned intrinsic disadvantages is combining active transition metal oxide hydroxides nanostructures with MXenes. Unfortunately, numerous studies have not proved it to be a straightforward endeavor as this might cause process complications and material deterioration when it is done in an uncontrollable way.

In recent years, there have been quite a few successful demonstrations of reactive surface modification (RSM) strategy in the preparation of multifunctional MXene-based nanohybrids. For instance, the in situ sulfidation of $\text{Mo}_2\text{TiC}_2\text{T}_x$ MXene has successfully turned the precursor into a MoS_2 -on-MXene heterostructure by utilizing its abundant surface-exposed metal sites, which demonstrated the great potential of the RSM strategy.¹⁹ On the other hand, the RSM process was also deployed for the synthesis of various transition metal sulfide, trichalcogenidophosphates, and alloy modified MXene nanohybrids with additional metal source.²⁰⁻²⁴ In particular, the strong affinity between the modified species and the surface metal atoms of MXenes can also be observed. Unfortunately, the major drawback of the RSM process is the rapid consumption of the surface-exposed metal atoms on MXenes, make it a stringent requirement for the RSM process. On top of that, the structural stability problem arises from the migration of metal atoms from the inner layer to the surface during the RSM process might screen out most of the frequently used MXenes

with general formulas of M_2X and M_3X_2 (M = early transition metals; X = C, N).

Taking the aforementioned considerations into account, we synthesized a novel MXene-based catalyst with nine atomic layers, namely $\text{V}_4\text{C}_3\text{T}_x$ MXene. The multilayered $\text{V}_4\text{C}_3\text{T}_x$ presented excellent structural stability during the RSM process. In addition, the OER performance of the $\text{V}_4\text{C}_3\text{T}_x$ MXene and its RSM derivatives were evaluated. After the in situ surface transformation during OER process, a series of nanohybrids that consist of $\text{V}_4\text{C}_3\text{T}_x$ MXene with Ni/Fe/V-ternary oxide hydroxides thin layer surface modification (denoted as $\text{MOOH}@V_4\text{C}_3\text{T}_x$, M = Ni, Fe, and V) were obtained. With the optimized Ni/Fe ratio, the nanohybrid delivered the lowest overpotential (η) of 275.2 mV at a current density of 10 mA cm^{-2} , which is comparable to most of the state-of-the-art noble metal-contained or noble metal-free OER catalysts. Finally, with the high OER activity of the surface ternary oxide hydroxide layers and the stable conductive skeleton of the $\text{V}_4\text{C}_3\text{T}_x$ MXene, $\text{V}_4\text{C}_3\text{T}_x$ -based nanohybrid revealed excellent stability over 70-hours long-time OER process.

The $\text{V}_4\text{C}_3\text{T}_x$ MXene was obtained via the HF selective etching method from the bulk V_4AlC_3 MAX phase (Figure 1A, for detail, see Supporting Information).²⁵ The phase purity of each product was verified by the powder X-ray diffraction (XRD) technique. As shown in Figure 1B, the XRD pattern of the bulk V_4AlC_3 was in accordance with the corresponding simulated pattern from the single-crystal X-ray data of V_4AlC_3 .²⁶ After HF etching, three new broad peaks of (002), (004), and (008) plane ($2\theta \approx 7.0^\circ$, 14.6° , and 29.7° , respectively) from $\text{V}_4\text{C}_3\text{T}_x$ phase appeared. After centrifugation, highly pure $\text{V}_4\text{C}_3\text{T}_x$ can be isolated, which was evidenced by seeing only one strong (002) peak located at $2\theta \approx 5.3^\circ$.²⁵ The scanning electron microscopy (SEM) and transmission electron microscopy (TEM) were then applied to characterize the morphology of the products (Figure 1C-E). From the SEM, the V_4AlC_3 powder presented a bulk morphology (Figure 1C), while the HF etched V_4AlC_3 showed a typical accordion-like structure (Figure 1D), indicating the successful removal of interlamellar Al atoms from the V_4AlC_3 lattice. After ultrasonic exfoliation, the purified $\text{V}_4\text{C}_3\text{T}_x$ nanosheet can be obtained (Figure 1E). Moreover, the TEM image of an isolated $\text{V}_4\text{C}_3\text{T}_x$ nanosheet showed the multilayered structure (Figure 1F), which was in accordance with the SEM results. The phase of the $\text{V}_4\text{C}_3\text{T}_x$ MXene was also confirmed by TEM. The fast Fourier transformation (FFT) pattern and the inverse FFT image of the selected area highlighted in Figure 1F are shown in Figure 1G. From the FFT pattern, single-crystalline nature of the $\text{V}_4\text{C}_3\text{T}_x$ nanosheets can be confirmed. In addition, a series of lattice planes can be identified from the inverse FFT image. As labeled in

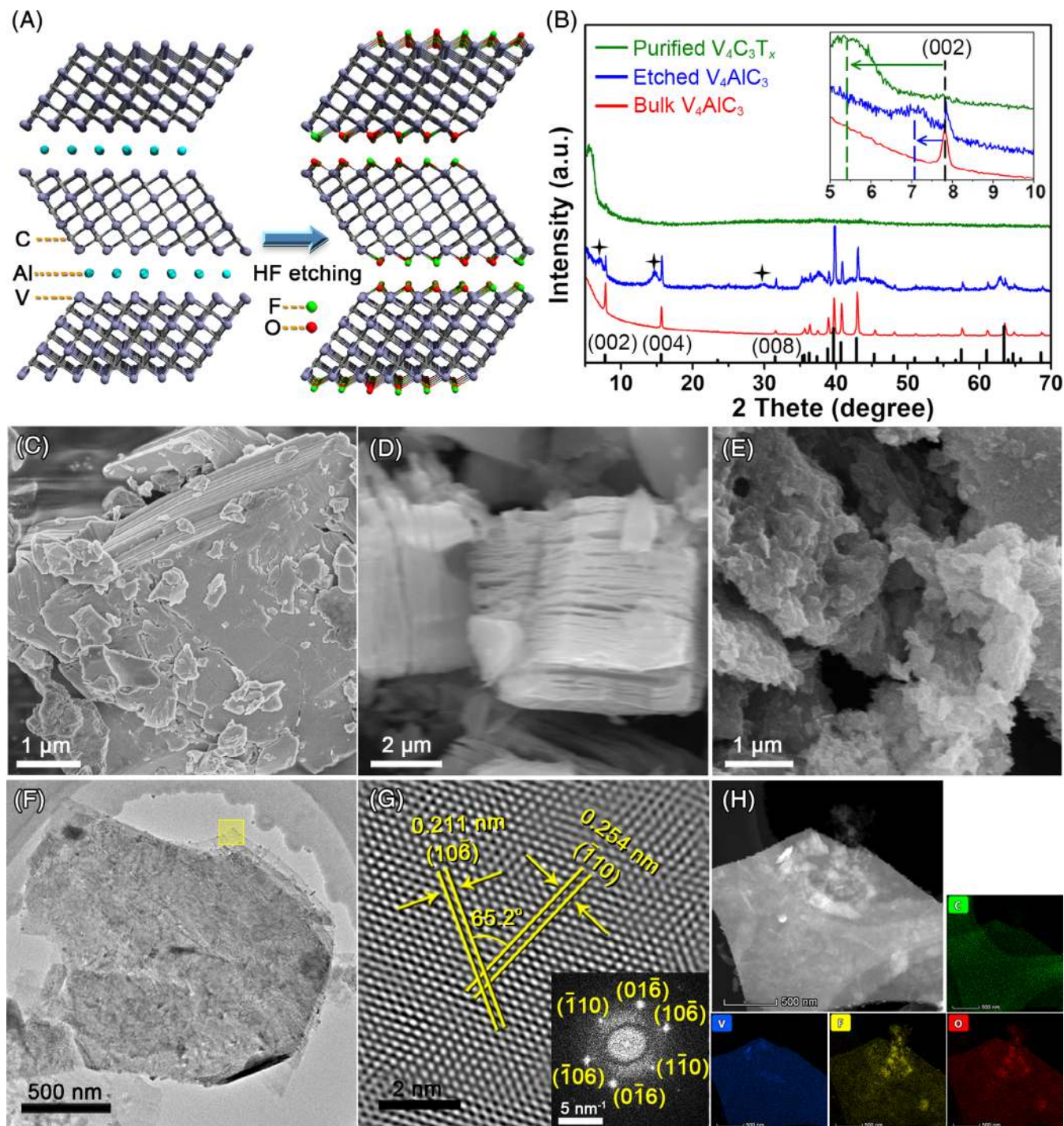


FIGURE 1 A, Schematic illustration showing the HF etching and exfoliation of $V_4C_3T_x$ MXene with nine atomic layers. B, XRD patterns of the bulk V_4AlC_3 , the HF etched V_4AlC_3 , and the purified $V_4C_3T_x$. C, SEM image of bulk V_4AlC_3 . D, SEM image of the HF etched V_4AlC_3 . E, SEM image and, F, TEM images of the purified $V_4C_3T_x$ MXene. G, The FFT patterns (inserted) and the inverse FFT image of the selected area highlighted in (F). H, The EDX elemental mapping of $V_4C_3T_x$ MXene. EDX, energy dispersive X-ray spectroscopy; FFT, fast Fourier transformation; SEM, scanning electron microscopy; TEM, transmission electron microscopy; XRD, X-ray diffraction

Figure 1G, two lattice planes with inter-lattice distances of 0.254 and 0.211 nm can be assigned to the $\{\bar{1}10\}$ and $\{10\bar{6}\}$ planes of the $V_4C_3T_x$, respectively. The homogeneous distribution of V, C, F, and O in the $V_4C_3T_x$ nanosheets were also confirmed by the energy dispersive

X-ray spectroscopy (EDX) elemental mapping under TEM (Figure 1H).

While for the RSM- $V_4C_3T_x$ nanoprecursors, facile self-assembly, and thermal reduction process were applied (for detail, see Supporting Information).^{21,22} For nanohybrids

with varied Ni/Fe ratios in precursors, their contents were further confirmed by inductively coupled plasma-atomic emission spectrometry (ICP-AES) analysis. The atomic ratio of Ni, Fe, and $V_4C_3T_x$ in each sample was calculated (Table S1), which were in accordance with those starting materials. According to the ICP analysis, the RSM- $V_4C_3T_x$ nanoprecursors with different alloy compositions were denoted as $M_1@V_4C_3T_x$, $M_2@V_4C_3T_x$, $M_3@V_4C_3T_x$, and $M_4@V_4C_3T_x$. The phase purity of RSM- $V_4C_3T_x$ nanoprecursors was also confirmed by XRD. As shown in Figure S1A, the nanocomposites consisted of Ni metal phase (JCPDS No. 87-0712) and V_4C_3 phase (JCPDS No. 89-5055). Obviously, with the increase of Fe content, the peaks of (111) and (200) planes arise from alloy were weakened and broadened, whereas the (111) and (220) planes arise from $V_4C_3T_x$ remained nearly unchanged. The XRD patterns indicated a decrease in the size of alloy with the increasing content of Fe. While for the control samples that were synthesized without $V_4C_3T_x$ MXene (Figure S1B), peaks of (111) and (200)

planes arise from the alloy became much sharper, indicating a drastic increase in grain size after thermal reduction. Figure 2A,B showed the SEM images of the $M_3@V_4C_3T_x$ nanoprecursor before and after thermal reduction, respectively. From the SEM, the porous morphology of the nanoprecursor was fully maintained. EDX elemental mapping was also applied to verify the homogeneous distribution of each element in the sample (Figure 2C). The TEM and high-resolution TEM (HRTEM) images of the nanoprecursor are shown in Figure 2D,E, respectively. As shown in Figure 2D, the layered structure can be clearly observed at low magnification. From the HRTEM image, the grains of alloy with a diameter of around 10 nm were randomly attached on the surface of the $V_4C_3T_x$ nanosheets (Figure 2E). The corresponding inverse FFT images of the $V_4C_3T_x$ substrate and the alloy grain were shown in Figure 2F,G, respectively. As labeled in Figure 2F, the lattice planes with inter-lattice distances of 0.202 nm can be identified. The two lattice planes were ascribed to the {200} planes

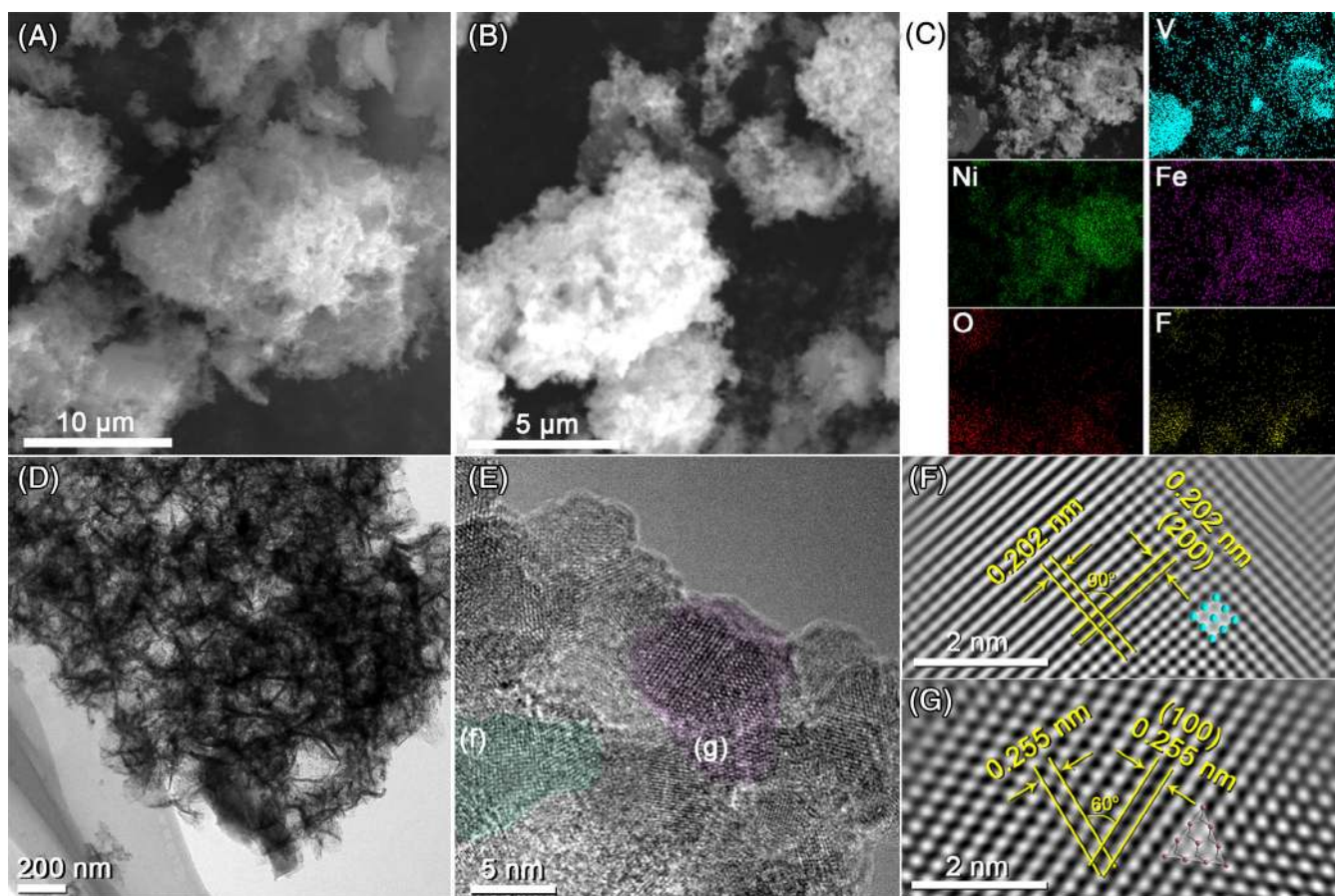


FIGURE 2 SEM images of the RSM nanoprecursor for $M_3OOH@V_4C_3T_x$. A, before thermal reduction and, B, after thermal reduction. C, The EDX elemental mapping of (B). D, TEM images of the nanoprecursor. E, The HRTEM image of the nanoprecursor. F and G, Show the inverse FFT images of the regions labeled in (E). EDX, energy dispersive X-ray spectroscopy; FFT, fast Fourier transformation; HRTEM, high-resolution TEM; RSM, reactive surface modification; SEM, scanning electron microscopy; TEM, transmission electron microscopy

of the NiO phase (JCPDS No. 78-0643), which might be originated from the surface oxidation of the highly active alloy nanoparticles. In addition, for the inverse FFT images of the $V_4C_3T_x$ substrate shown in Figure 2G, the lattice planes with inter-lattice distances of 0.255 nm corresponded to the {100} plane of $V_4C_3T_x$, which confirmed the presence of $V_4C_3T_x$ MXene and was consistent with the XRD results.

In order to get further insight into the feature of chemical bonding on the surface of the $V_4C_3T_x$ MXene and RSM- $V_4C_3T_x$ nanoprecursors, X-ray photoelectron spectroscopy (XPS) of the $V_4C_3T_x$ MXene were performed (Figure 3A-D). For the $V_4C_3T_x$ MXene, the high-resolution XPS signals of V 2p spectrum can be deconvoluted into five peaks. As shown in Figure 3A, the peak centered at 513.3 eV was related to the binding energy of V-C species.²⁷ The other four peaks were related to the V^{2+} (514.0 and 521.1 eV) and V^{3+} (516.0 and 523.1 eV) species, respectively.^{27,28} In the C 1s spectrum (Figure 3B), the binding energy at 282.4 eV confirmed the presence of C-V species.^{27,29} While the other three peaks centered at 284.7, 286.3, and 287.1 eV

corresponding to the adventitious contaminations.²⁷ For the O 1s spectrum (Figure 3C), four peaks centered at 529.6, 530.5, 532.3, and 534.8 eV can be deconvoluted. For the peak deconvolution of the O 1s spectrum, peaks centered at 530.5 and 532.3 eV can be assigned to the C-V-OH and C-V-O_x species.²⁷ The peak at 529.6 eV was related to the surface metal oxide species,³⁰ whereas binding energy of 534.8 eV might be related to the surface adsorbed water.^{31,32} The F 1s spectrum can be deconvoluted into two peaks (Figure 3D), which might arise from the surface C-V-F_x (683.8 eV) and other F contained species (686.4 eV).²⁰

In comparison, the high-resolution XPS signals of V 2p, C 1s, O 1s, and F 1s spectra from the RSM- $V_4C_3T_x$ nanoprecursor are also shown in Figure 3. For the deconvoluted V 2p peak, the binding energy of 512.8 eV corresponded to the V-C species, indicating the retention of $V_4C_3T_x$ skeleton. Compared with the V 2p spectrum of the $V_4C_3T_x$ MXene, the intensity of the two peaks related to V^{3+} (516.0 and 522.0 eV) increased while the peak related to V^{2+} (514.4 eV) decreased (Figure 3E). The results indicated that the surface V species were also

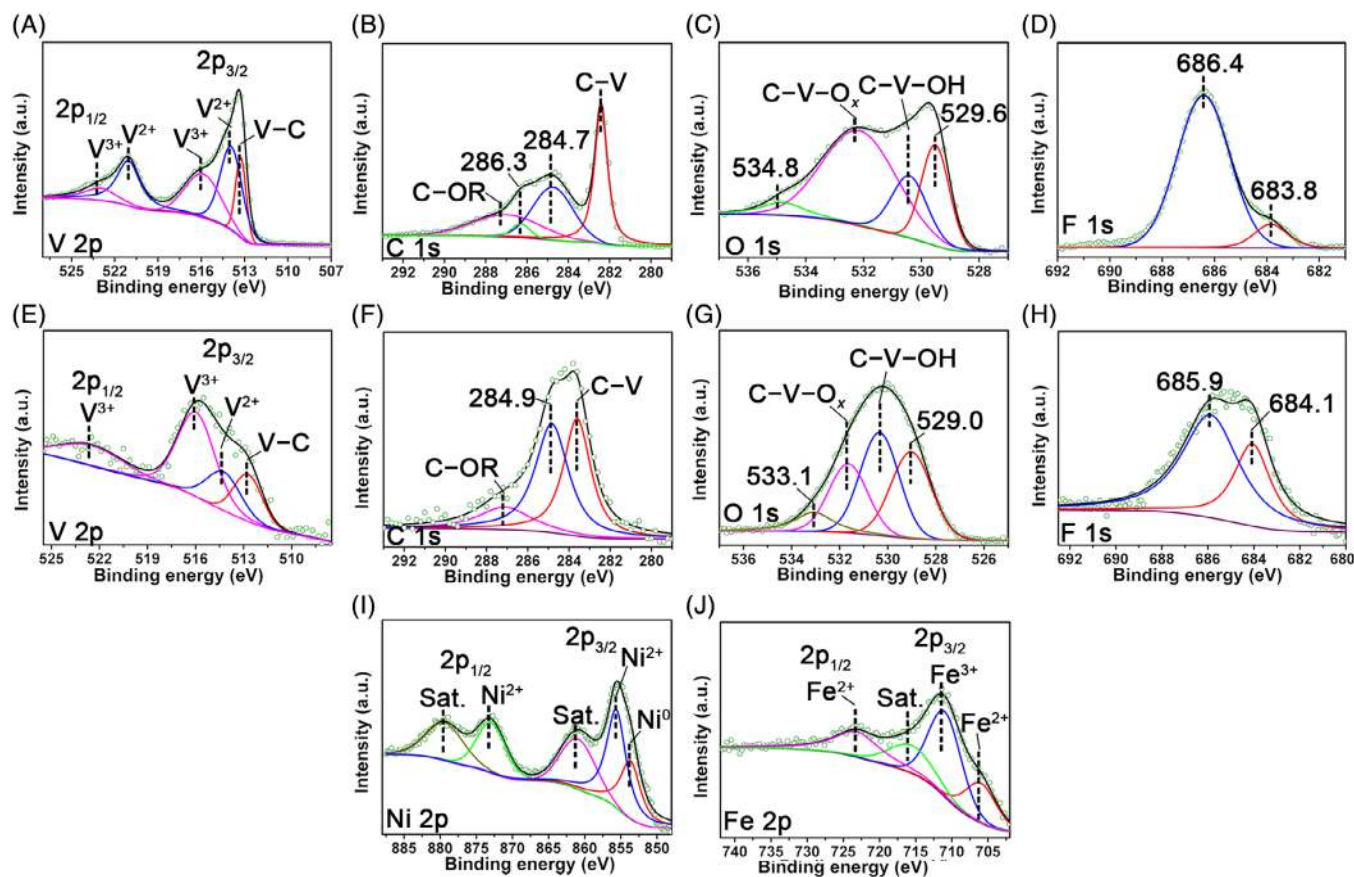


FIGURE 3 XPS spectra of, A, V 2p; B, C 1s; C, O 1s; D, F 1s from the $V_4C_3T_x$ MXene; E, V 2p; F, C 1s; G, O 1s; H, F 1s; I, Ni 2p; J, Fe 2p from the RSM- $V_4C_3T_x$ nanoprecursor with Ni:Fe ratio of around 4:1. RSM, reactive surface modification; XPS, X-ray photoelectron spectroscopy

involved in the RSM. For the C 1s spectrum (Figure 3F), the deconvoluted peak centered at 283.6 eV can be assigned to the binding energy of C-V species.^{27,29} Similarly, the other two peaks at 284.9 and 287.2 eV were related to the adventitious contaminations.²⁷ The O 1s spectrum can also be deconvoluted into four peaks (Figure 3G). The first three peaks still related to the surface metal oxide species (529.0 eV), C-V-OH (530.4 eV) and C-V-O_x species (531.7 eV), respectively.²⁷ And the peak at 533.1 eV was corresponded to the surface adsorbed water.^{31,33} Similarly, the F 1s spectrum can be deconvoluted into two peaks (Figure 3H), which belonged to the surface C-V-F_x component (684.1 eV) and other F contained species (685.9 eV).²⁰ Additionally, the XPS spectra of Ni 2p and Fe 2p from the nanoprecursor were also acquired. As shown in Figure 3I, the Ni 2p spectrum can be deconvoluted into five peaks. The peak at 853.8 eV was assigned to the 2p_{3/2} core level of Ni⁰,²² whereas the peaks at 855.7 and 873.2 eV were related to the Ni²⁺ species.³⁴ The two peaks at 861.2 and 879.7 eV were the satellite peaks of the Ni 2p_{1/2} and 2p_{3/2} core levels, respectively.^{34,35} For the Fe 2p spectrum (Figure 3J), the two deconvoluted peaks located at 706.4 and 723.4 eV were related to the Fe²⁺ species.³⁴ While the peak at 711.3 eV indicated the presence of Fe³⁺ species.^{11,36} The satellite peak of Fe 2p_{3/2} core level was located at 716.2 eV.³⁵

As demonstrated by some in situ studies, the surface of electrocatalyst will go through a reformation, thus forming the surface metal hydroxides/oxide hydroxides (MOOH) species which might be the indeed OER active species during OER process.^{8-10,37} For the RSM-V₄C₃T_x nanoprecursors, the surface alloy nanoparticles were also expected to be the sacrificial templates, which can undergo in situ generation of MOOH species anchoring on the surface of V₄C₃T_x MXene. Therefore, cyclic voltammetry (CV) was first applied to evaluate the surface reformation behaviors of the RSM-V₄C₃T_x nanoprecursors and V₄C₃T_x MXene under high applied potential. As shown in Figure S2, all the RSM-V₄C₃T_x nanoprecursors exhibited enhanced OER activities after CV cycles in 1 M KOH solution. And the broad redox peaks observed in the first CV cycle (related to the V₄C₃T_x MXene) gradually decreased as the Fe content increased. The stable redox peaks observed from all the CV curves related to RSM-V₄C₃T_x nanoprecursors were similar to other reported Ni/Fe containing OER catalysts,^{38,39} which suggested the surface transformation during OER process and generation of surface MOOH layers.

Based on the morphology and CV analyses, the electrocatalytic OER performance of the V₄C₃T_x MXene and the series of MOOH@V₄C₃T_x nanohybrids were carefully evaluated by linear sweep voltammetry (LSV) in

1 M KOH solution (Figure 4A, Figures S3A,3B). The Ohmic potential drop was also corrected. As plotted in Figure 4A, the pristine V₄C₃T_x MXene showed nearly no OER activity in the potential window being tested. However, the surface-modified V₄C₃T_x MXenes all showed an enhanced OER activity. Particularly, the M₃OOH@V₄C₃T_x nanohybrid only needed an overpotential (η) of 275.2 mV to reach a current density of 10 mA cm⁻², which depicted the lowest overpotential among all the tested MOOH@V₄C₃T_x samples including M₁OOH@V₄C₃T_x (η = 303.9 mV), M₂OOH@V₄C₃T_x (η = 290.6 mV), M₄OOH@V₄C₃T_x (η = 286.5 mV), and the commercial noble metal-based IrO₂ catalyst (η = 311.4 mV). For the bare MOOH and MOOH obtained from Ni/Fe alloy (denoted as MOOH@M), the same Ni/Fe ratio as the corresponding MOOH@V₄C₃T_x nanohybrids, LSV data were also collected. As plotted in Figure 4A, the MOOH@V₄C₃T_x nanohybrids showed a lower η than most of the control samples, whereas the M₃OOH@M₃ and M₄OOH@M₄ present the comparable η with the M₃OOH@V₄C₃T_x. Evidenced by the SEM analysis, the 2D structures of the four MOOH@V₄C₃T_x nanohybrids were still maintained after the OER process (Figure S3C-D). In order to probe the OER kinetics of the serial samples, Tafel plots were calculated from the corresponding LSV curves. As shown in Figure 4B and Figure S3B, the M₁OOH@V₄C₃T_x, M₂OOH@V₄C₃T_x, M₃OOH@V₄C₃T_x, and M₄OOH@V₄C₃T_x presented the Tafel slopes of 51.6, 50.0, 51.4, and 51.9 mV dec⁻¹, respectively, which were all lower than the bare V₄C₃T_x MXene (122.9 mV dec⁻¹), commercial IrO₂ catalyst (71.9 mV dec⁻¹), MOOH@M and bare MOOH (>100 mV dec⁻¹). From the Tafel slopes, all of the MOOH@V₄C₃T_x nanohybrids presented faster OER kinetics than the samples without V₄C₃T_x MXene. In order to get a further insight into the role of V₄C₃T_x MXene in promoting the OER activity, electrochemical impedance spectroscopy was performed on the V₄C₃T_x MXene, MOOH@V₄C₃T_x nanohybrids, and the MOOH@M samples. As shown in Figure 4C, evidenced by the Nyquist plots, the samples with V₄C₃T_x MXene all presented a reduced radius of the semicircle at the high-frequency region, indicating a lower charge transfer resistance (R_{ct}). Therefore, the enhanced OER activity of MXene-containing nanohybrids can be partly ascribed to the rapid charge transfer kinetics of the highly conductive network constructed by MXene nanosheets. Since the critical Fe³⁺ content in NiOOH matrix was around 25% to keep the homogeneous Ni_{1-x}Fe_xOOH structure,⁴⁰ the best OER performance of M₃OOH@V₄C₃T_x nanohybrid might be ascribed to the rich Fe substituted site with a homogeneous structure and the fast charge transfer network of MXene substrate. Noteworthy, the low overpotential and Tafel slope of the as-prepared MOOH@V₄C₃T_x nanohybrid is

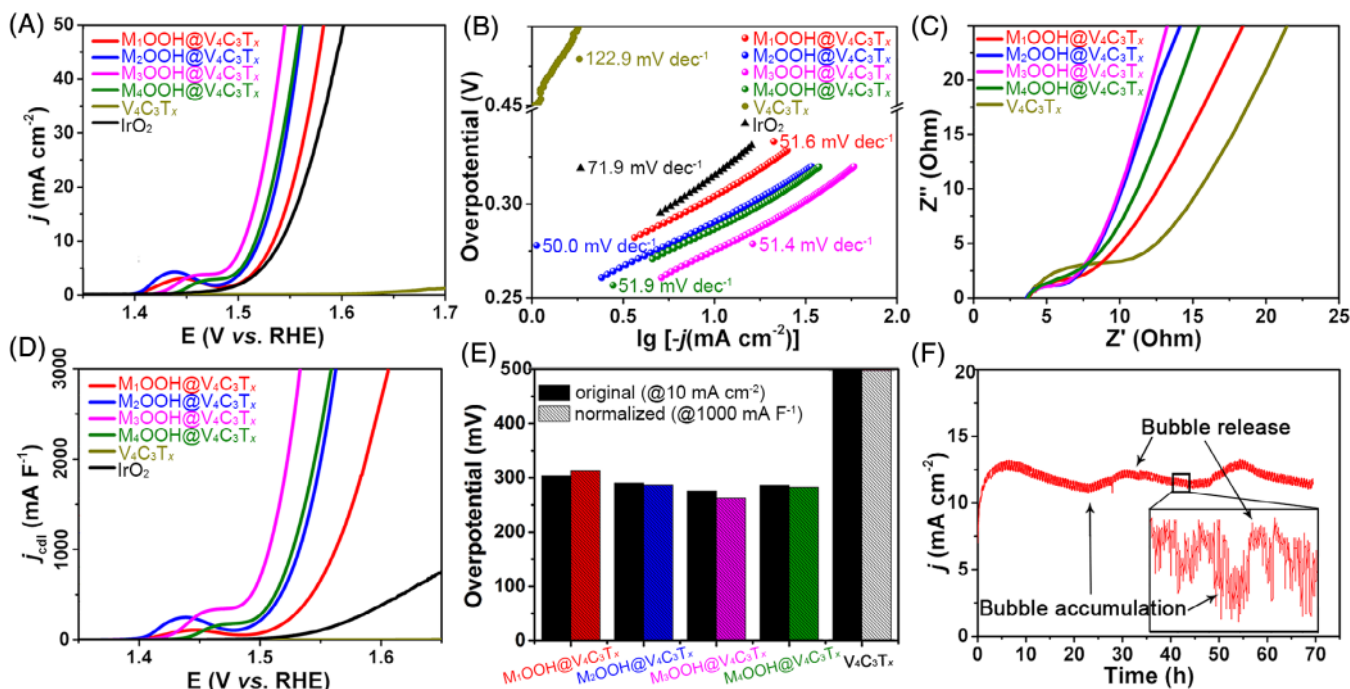


FIGURE 4 A, OER polarization curves of $V_4C_3T_x$ MXene, the series $MOOH@V_4C_3T_x$ nanohybrids, and commercial IrO_2 catalyst in 1 m KOH with a scan rate of 5 mV s^{-1} . B, Corresponding Tafel plots of the series samples. C, Nyquist plots of $V_4C_3T_x$ MXene and the series $MOOH@V_4C_3T_x$ nanohybrids measured at the potential of 0 V vs RHE. D, Normalized OER polarization curves shown in (A) by the C_{dl} . E, The η and $\eta_{C_{dl}}$ of $V_4C_3T_x$ MXene and the series $MOOH@V_4C_3T_x$ nanohybrids. F, The chronoamperometry curves of the $M_3OOH@V_4C_3T_x$ nanohybrid at a static potential with current density of around 10 mA cm^{-2} over 70 hours. OER, oxygen evolution reaction

comparable or even better than some of the state-of-the-art noble metal-contained or non-noble metal-based OER electrocatalysts, such as $N-CO_3O_4@NC-2$ ($\eta = 266\text{ mV}@54.9\text{ mV dec}^{-1}$),⁴¹ Raney NiO_x ($\eta = 304\text{ mV}@53\text{ mV dec}^{-1}$),⁴² $Ir_1@Co/NC$ ($\eta = 260\text{ mV}@163\text{ mV dec}^{-1}$),⁴³ and $CoCo-LDH\ 2D$ nanomesh ($\eta = 319\text{ mV}@42\text{ mV dec}^{-1}$).⁴⁴ When compared with the recent reported MXene-based OER electrocatalysts, for example, $FeNi-LDH/Ti_3C_2-MXene$ ($\eta = 298\text{ mV}@43\text{ mV dec}^{-1}$),⁴⁵ peeled off $NiFe-LDH/MXene$ powder ($\eta = 314\text{ mV}@67\text{ mV dec}^{-1}$),⁴⁶ $NiCoS/Ti_3C_2T_x$ ($\eta = 365\text{ mV}@153.1\text{ mV dec}^{-1}$),⁴⁷ and the $Co/N-CNTs@Ti_3C_2T_x$ ($\eta = 411\text{ mV}@79.1\text{ mV dec}^{-1}$),⁴⁸ the nanohybrid reported in this study also delivers lower overpotential and faster OER kinetics.

In order to explore the intrinsic property variations of the $MOOH@V_4C_3T_x$ nanohybrid, $NiOOH$ monolayer (001)-surface adsorbed on O-terminated $V_4C_3O_2$ monolayer was taken as the model structure for density functional theory simulation (Figure S4A). As a result, the optimized interlayer spacing was only 1.464 \AA with a binding energy of -0.079 eV per unit cell (the area of a supercell is 32.60 \AA^2), which indicated an appreciable electronic coupling between $NiOOH$ and $V_4C_3O_2$ layers. As confirmed by the total density of states (TDOS) results (Figure S4B), the $NiOOH$, $V_4C_3O_2$, $NiOOH@V_4C_3O_2$, Fe-doped $NiOOH@V_4C_3O_2$, and V-doped $NiOOH@V_4C_3O_2$

nanohybrids were all present continuous TDOS near the Fermi levels, revealing the intrinsically metallic features thus possessing fast charge transfer and showing higher electron conductivity. Additionally, as shown in Figure S4B, the peak from low electrical states of bare $NiOOH$ shifted to the Fermi level after $NiOOH$ stacked with $V_4C_3O_2$, suggesting an enhancement on electrical states at the Fermi level and a stronger carrier density.

It should be pointed out that the electrocatalytic activity is usually proportional to the surface area. Therefore, the electrochemical double-layer capacitance (C_{dl}) of the $V_4C_3T_x$ MXene and $MOOH@V_4C_3T_x$ nanohybrids were determined to evaluate their electrochemically effective surface area. As shown in Figures S5 and S6, the pristine $V_4C_3T_x$ MXene presented the highest C_{dl} area (25.12 mF cm^{-2}) among all the tested samples, which was around 2- to 8-fold larger than the $MOOH@V_4C_3T_x$ nanohybrids. For four $MOOH@V_4C_3T_x$ nanohybrids, the $M_3OOH@V_4C_3T_x$ gave the smallest C_{dl} area (2.18 mF cm^{-2}). Hence, the LSV curves of all the samples were normalized by the corresponding C_{dl} area in order to evaluate their real OER activities. As shown in Figure 4D and Figure S6B, the normalized LSV curves presented a similar tendency as shown in Figure 4A and Figure S3A. In order to better evaluate the relationship between C_{dl} area and OER activities, the normalized overpotential for

each MOOH@V₄C₃T_x nanohybrid to reach the $j_{C_{dl}}$ of 1000 mA F⁻¹ was chosen as the standard. Interestingly, it was found that, although the normalized overpotentials ($\eta_{C_{dl}}$) of the M₂OOH@V₄C₃T_x, M₃OOH@V₄C₃T_x, and M₄OOH@V₄C₃T_x were all lower than the original ones, the $\eta_{C_{dl}}$ of M₁OOH@V₄C₃T_x was higher than the original value (Figure 4E). The estimated turnover frequencies of the MOOH@V₄C₃T_x, MOOH@M, and IrO₂ catalysts also confirmed the higher intrinsic OER activities of the MOOH@V₄C₃T_x nanohybrids (Figure S6C). These results implied that the enhancement of OER performance after Ni/Fe RSM on V₄C₃T_x MXene might be related to the higher intrinsic activity of the suitable Ni/Fe ratio and the synergy of the V₄C₃T_x MXene substrate.

Finally, the chronoamperometry curve of the optimized M₃OOH@V₄C₃T_x nanohybrid was recorded at a static potential with current density of around 10 mA cm⁻² over 70 hours to evaluate the stabilities of the nanohybrid (Figure 4F). After the 70-hours OER process, the current density remained almost the same. As observed in the XRD pattern, the tested sample presented an amorphous nature (Figure S7). Therefore, TEM and HRTEM images of the nanohybrid after 70-hours OER process were taken for further verification. As shown in Figure S8, the lattice pattern of the V₄C₃T_x substrate can still be identified from the HRTEM and inverse FFT image, indicating the good stability of the V₄C₃T_x MXene. However, many thin amorphous patches were covered on the surface of V₄C₃T_x MXene, which can be ascribed to the surface MOOH species. To characterize the variation in chemical bonding of the nanohybrid and verify the products, XPS was performed again on the materials after 70-hours OER process. As shown in the XPS spectra (Figure S9), after the long-time OER process, the signals of C-V and C-V-F_x components can still be detected from the C 1s and the F 1s spectra. While for the O 1s spectrum, signals of surface metal oxide species (529.3 eV), C-V-OH (530.2 eV), C-V-O_x (531.1 eV) species, and surface adsorbed water (532.0 eV) were still detected, respectively.^{27,31} And a new deconvoluted peak located at 528.4 eV appeared, which is possibly related to the surface MOOH species. For Ni 2p, the deconvoluted peak of Ni⁰ disappeared and only Ni²⁺ signal can be detected. In addition, in V 2p and Fe 2p spectra, the deconvoluted peaks for V³⁺ (516.2 and 522.9 eV) and Fe³⁺ (712.1 and 734.1 eV) became stronger,^{11,49} indicating that V³⁺ and Fe³⁺ species might exist in the MOOH surface layers as dopant after the surface oxidation reaction.

In summary, a novel nine atomic layered V₄C₃T_x MXene was obtained via the HF etching method, for which the multilayered structure endowed it with excellent structural stability during RSM and OER processes. By utilizing the reactive surface alloy modified V₄C₃T_x

MXene as nanoprecursor, a series of MOOH@V₄C₃T_x (M = Ni, Fe, and V) nanohybrids were successful obtained via in situ surface transformation during the OER process. Owing to the high OER activity of the surface ternary oxide hydroxide layers and the stable conductive skeleton of the V₄C₃T_x MXene, these nanohybrids present excellent OER activity and durability. With an optimized Ni/Fe ratio, the nanohybrid delivered a very low η of 275.2 mV, and excellent stability over 70-hours long-time OER process. Demonstrated by the tunable physicochemical properties and excellent structural stability of these nanohybrids, the multilayered M₄X₃-based MXenes show great promise as efficient substrates for future energy conversion and storage applications.



ACKNOWLEDGMENTS

The calculation was carried out at National Supercomputer Center in Tianjin, and performed on TianHe-1(A). The authors gratefully acknowledge the financial support from Singapore MOE Tier 2 MOE2017-T2-2-069 and MOE2018-T2-1-010. The National Natural Science Foundation of China (No. 51901189), the “Shuimu Tsinghua Scholar Program” and the Opening Project of Key Laboratory of Materials Processing and Mold (No. NERC201903). The authors also acknowledge the Facility for Analysis, Characterization, Testing and Simulation (FACTS), Nanyang Technological University, Singapore, for use of the XPS Kratos AXIS Supra facilities; the Analytical & Testing Center of Northwestern Polytechnical University, for use of the SEM Helios G4 CX microscope; and the Shaanxi Materials Analysis and Research Center for use of the TEM Talos F200X facilities.

CONFLICT OF INTEREST

The authors have no conflict of interest to report.

ORCID

Cheng-Feng Du  <https://orcid.org/0000-0002-5598-476X>
Qingyu Yan  <https://orcid.org/0000-0003-0317-3225>

REFERENCES

- Xiao Z, Wang Y, Huang Y-C, et al. Filling the oxygen vacancies in Co₃O₄ with phosphorus: an ultra-efficient electrocatalyst for overall water splitting. *Energ Environ Sci*. 2017;10(12):2563-2569.
- Sun Y, Xu K, Wei Z, et al. Strong electronic interaction in dual-cation-incorporated NiSe₂ nanosheets with lattice distortion for highly efficient overall water splitting. *Adv Mater*. 2018;30(35):1802121.
- Du C-F, Liang Q, Dangol R, et al. Layered trichalcogenidophosphate: a new catalyst family for water splitting. *Nano-Micro Lett*. 2018;10(4):67.

- Roger I, Shipman MA, Symes MD. Earth-abundant catalysts for electrochemical and photoelectrochemical water splitting. *Nat Rev Chem*. 2017;1:0003.
- Liu S, Wang M, Sun X, et al. Zinc-air batteries: facilitated oxygen chemisorption in heteroatom-doped carbon for improved oxygen reaction activity in all-solid-state zinc-air batteries. *Adv Mater*. 2018;30(4):1870028.
- Liu Z, Wang Y, Chen R, et al. Quaternary bimetallic phosphosulphide nanosheets derived from prussian blue analogues: origin of the ultra-high activity for oxygen evolution. *J Power Sources*. 2018;403:90-96.
- Chen Y, Zhou Q, Zhao G, et al. Electrochemically inert g-C₃N₄ promotes water oxidation catalysis. *Adv Funct Mater*. 2018;28(5):1705583.
- Konkena B, Masa J, Botz AJR, et al. Metallic NiPS₃@NiOOH core-shell heterostructures as highly efficient and stable electrocatalyst for the oxygen evolution reaction. *ACS Catal*. 2017;7(1):229-237.
- Ye S-H, Shi Z-X, Feng J-X, Tong Y-X, Li G-R. Activating CoOOH porous nanosheet arrays by partial iron substitution for efficient oxygen evolution reaction. *Angew Chem Int Ed*. 2018;57(10):2672-2676.
- Jayaramulu K, Masa J, Morales DM, et al. 2D metal-organic frameworks: ultrathin 2D cobalt zeolite-imidazole framework nanosheets for electrocatalytic oxygen evolution. *Adv Sci*. 2018;5(11):1870072.
- Zhang Y, Rui K, Ma Z, et al. Cost-effective vertical carbon nanosheets/iron-based composites as efficient electrocatalysts for water splitting reaction. *Chem Mater*. 2018;30(14):4762-4769.
- Yu H, Wang Y, Jing Y, Ma J, du CF, Yan Q. Surface modified MXene-based nanocomposites for electrochemical energy conversion and storage. *Small*. 2019;15(25):1901503.
- Pang J, Mendes RG, Bachmatiuk A, et al. Applications of 2D MXenes in energy conversion and storage systems. *Chem Soc Rev*. 2019;48(1):72-133.
- Xiong D, Li X, Bai Z, Lu S. Recent advances in layered Ti₃C₂T_x MXene for electrochemical energy storage. *Small*. 2018;14(17):e1703419.
- Mendoza-Sánchez B, Gogotsi Y. Synthesis of two-dimensional materials for capacitive energy storage. *Adv Mater*. 2016;28(29):6104-6135.
- Gao G, O'Mullane AP, Du A. 2D MXenes: a new family of promising catalysts for the hydrogen evolution reaction. *ACS Catal*. 2017;7(1):494-500.
- Li Z, Wu Y. 2D early transition metal carbides (MXenes) for catalysis. *Small*. 2019;15(29):e1804736.
- Meshkian R, Dahlqvist M, Lu J, et al. W-based atomic laminates and their 2D derivative W1₃₃C MXene with vacancy ordering. *Adv Mater*. 2018;30(21):e1706409.
- Chen C, Xie X, Anasori B, et al. MoS₂-on-MXene heterostructures as highly reversible anode materials for lithium-ion batteries. *Angew Chem*. 2018;130(7):1864-1868.
- Du C-F, Liang Q, Zheng Y, et al. Porous MXene frameworks support pyrite nanodots toward high-rate pseudocapacitive Li/Na-ion storage. *ACS Appl Mater Interfaces*. 2018;10(40):33779-33784.
- Du C-F, Dinh KN, Liang Q, et al. Self-assemble and in situ formation of Ni_{1-x}Fe_xPS₃ nanomosaic-decorated MXene hybrids for overall water splitting. *Adv Energy Mater*. 2018;8(26):1801127.
- Du C-F, Sun X, Yu H, et al. Synergy of Nb doping and surface alloy enhanced on water-alkali electrocatalytic hydrogen generation performance in Ti-based MXene. *Adv Sci*. 2019;6(11):1900116.
- Li Z, Cui Y, Wu Z, et al. Reactive metal-support interactions at moderate temperature in two-dimensional niobium-carbide-supported platinum catalysts. *Nat Catal*. 2018;1(5):349-355.
- Zhang J, Zhao Y, Guo X, et al. Single platinum atoms immobilized on an MXene as an efficient catalyst for the hydrogen evolution reaction. *Nat Catal*. 2018;1(12):985-992.
- Wang X, Lin S, Tong H, et al. Two-dimensional V₄C₃ MXene as high performance electrode materials for supercapacitors. *Electrochim Acta*. 2019;307:414-421.
- Hu C, Zhang J, Wang J, Li F, Wang J, Zhou Y. Crystal structure of V₄AlC₃: a new layered ternary carbide. *J Am Ceram Soc*. 2008;91(2):636-639.
- Naguib M, Halim J, Lu J, et al. New two-dimensional niobium and vanadium carbides as promising materials for Li-ion batteries. *J Am Chem Soc*. 2013;135(43):15966-15969.
- VahidMohammadi A, Hadjikhani A, Shahbazmohamadi S, Beidaghi M. Two-dimensional vanadium carbide (MXene) as a high-capacity cathode material for rechargeable aluminum batteries. *ACS Nano*. 2017;11(11):11135-11144.
- Barsoum MW, Crossley A, Myhra S. Crystal-chemistry from XPS analysis of carbide-derived M_{n+1}AX_n (n=1) nano-laminate compounds. *J Phys Chem Solid*. 2002;63(11):2063-2068.
- Qin F, Zhao ZH, Alam MK, et al. Trimetallic NiFeMo for overall electrochemical water splitting with a low cell voltage. *ACS Energy Lett*. 2018;3(3):546-554.
- Liu J, Zhang HB, Sun R, et al. Hydrophobic, flexible, and lightweight MXene foams for high-performance electromagnetic-interference shielding. *Adv Mater*. 2017;29(38):1702367.
- Ran J, Gao G, Li FT, Ma TY, du A, Qiao SZ. Ti₃C₂ MXene cocatalyst on metal sulfide photo-absorbers for enhanced visible-light photocatalytic hydrogen production. *Nat Commun*. 2017;8:13907.
- Wang X, Sun P, Lu H, et al. Aluminum-tailored energy level and morphology of Co_{3-x}Al_xO₄ porous nanosheets toward highly efficient electrocatalysts for water oxidation. *Small*. 2019;15(11):1804886.
- Gu Y, Chen S, Ren J, et al. Electronic structure tuning in Ni₃FeN/r-GO aerogel toward bifunctional electrocatalyst for overall water splitting. *ACS Nano*. 2018;12(1):245-253.
- Rui K, Zhao G, Chen Y, et al. Hybrid 2D dual-metal-organic frameworks for enhanced water oxidation catalysis. *Adv Funct Mater*. 2018;28(26):1801554.
- Song B, Li K, Yin Y, et al. Tuning mixed nickel iron phosphosulfide nanosheet electrocatalysts for enhanced hydrogen and oxygen evolution. *ACS Catal*. 2017;7(12):8549-8557.
- Song S, Zhou J, Su X, et al. Operando X-ray spectroscopic tracking of self-reconstruction for anchored nanoparticles as high-performance electrocatalysts towards oxygen evolution. *Energ Environ Sci*. 2018;11(10):2945-2953.
- Jiang J, Sun FF, Zhou S, et al. Atomic-level insight into super-efficient electrocatalytic oxygen evolution on iron and vanadium co-doped nickel (oxy)hydroxide. *Nat Commun*. 2018;9:12.
- Wang J, Gan L, Zhang W, et al. In situ formation of molecular Ni-Fe active sites on heteroatom-doped graphene as a

- heterogeneous electrocatalyst toward oxygen evolution. *Sci Adv.* 2018;4(3):eaap7970.
40. Friebel D, Louie MW, Bajdich M, et al. Identification of highly active Fe sites in (Ni,Fe)OOH for electrocatalytic water splitting. *J Am Chem Soc.* 2015;137(3):1305-1313.
 41. Wang Z, Xu W, Chen X, et al. Defect-rich nitrogen doped Co₃O₄/C porous nanocubes enable high-efficiency bifunctional oxygen electrocatalysis. *Adv Funct Mater.* 2019;29:1902875.
 42. Delgado D, Bizzotto F, Zana A, Arenz M. Accelerated durability test for high surface area oxyhydroxide nickel (NiO_x) supported on Raney Nickel as catalyst for the alkaline oxygen evolution reaction. *ChemPhysChem.* 2019;20(22):3147-3153.
 43. Lai W, Zhang L, Hua W, et al. General pi-electron-assisted strategy for Ir, Pt, Ru, Pd, Fe, Ni single-atom electrocatalysts with bifunctional active sites toward highly efficient water splitting. *Angew Chem Int Ed.* 2019;58(34):11868-11873.
 44. Qin M, Li S, Zhao Y, et al. Unprecedented synthesis of holey 2D layered double hydroxide nanomesh for enhanced oxygen evolution. *Adv Energy Mater.* 2019;9(1):1803060.
 45. Yu M, Zhou S, Wang Z, Zhao J, Qiu J. Boosting electrocatalytic oxygen evolution by synergistically coupling layered double hydroxide with MXene. *Nano Energy.* 2018;44:181-190.
 46. Yu M, Wang Z, Liu J, et al. A hierarchically porous and hydrophilic 3D nickel-iron/MXene electrode for accelerating oxygen and hydrogen evolution at high current densities. *Nano Energy.* 2019;63:103880.
 47. Zou H, He B, Kuang P, Yu J, Fan K. Metal-organic framework-derived nickel-cobalt sulfide on ultrathin MXene nanosheets for electrocatalytic oxygen evolution. *ACS Appl Mater Interfaces.* 2018;10(26):22311-22319.
 48. Zhang Y, Jiang H, Lin Y, et al. In situ growth of cobalt nanoparticles encapsulated nitrogen-doped carbon nanotubes among Ti₃C₂T_x (MXene) matrix for oxygen reduction and evolution. *Adv Mater Interfaces.* 2018;5(16):1800392.
 49. Zhang Y, Jing X, Wang Q, et al. Hydrothermal synthesis and electrochemical properties of hierarchical vanadyl hydroxide spheres with hollow core and mesoporous shell. *Micropor Mesopor Mater.* 2017;249:137-145.

SUPPORTING INFORMATION

Additional supporting information may be found online in the Supporting Information section at the end of this article.

How to cite this article: Du C-F, Sun X, Yu H, et al. V₄C₃T_x MXene: A promising active substrate for reactive surface modification and the enhanced electrocatalytic oxygen evolution activity. *InfoMat.* 2020;2:950–959. <https://doi.org/10.1002/inf2.12078>